Oxygen vacancies enable the visible light photoactivity of chromium-implanted TiO_2 nanowires

Xianyin Song[a,1], Wenqing Li[a,1], Xiaojing Liu[b,1], Yishang Wu[b], Dong He[a], Zunjian Ke[a], Li Cheng[a], Changzhong Jiang[a], Gongming Wang[b,*], Xiangheng Xiao[a,*], Yat Li[c,*]

[a] *Department of Physics and Key Laboratory of Artificial Micro- and Nano-structures of Ministry of Education, Hubei Nuclear Solid Physics Key Laboratory, Wuhan University, Wuhan 430072, Hubei, China*

[b] *Department of Chemistry, University of Science and Technology of China, Hefei 230026, Anhui, China*

[c] *Department of Chemistry and Biochemistry, University of California, Santa Cruz, California 95064, United States*

[*]Corresponding authors.

E-mail addresses: xxh@whu.edu.cn (X. Xiao); wanggm@ustc.edu.cn (G. Wang); yatli@ucsc.edu (Y. Li).

[1]These authors contributed equally to this work.

ABSTRACT

Although computational studies have demonstrated that metal ion doping can effectively narrow the bandgap of TiO_2, the visible-light photoactivity of metal-doped TiO_2 photoanodes is still far from satisfactory. Herein, we report an effective strategy to activate the visible-light photoactivity of chromium-implanted TiO_2 *via* the incorporation of oxygen vacancies. The chromium-doped TiO_2 activated by oxygen vacancies (Cr-TiO_2-vac) exhibited an incident photon-to-electron conversion efficiency (IPCE) of ~6.8% at 450 nm, which is one of the best values reported for metal-doped TiO_2. Moreover, Cr-TiO_2-vac showed no obvious photocurrent decay

after 100 h under visible-light illumination.

Keywords: TiO_2 nanowires; Photoelectrochemical water splitting; Chromium implantation; Visible-light photoactivity

1. Introduction

Photoelectrochemical (PEC) water splitting is a promising strategy for the generation of solar hydrogen [1]. Although many photoactive materials have been extensively studied for PEC water splitting in the past decades [2–4], TiO_2 is still undoubtedly the most widely used photoanode material due to its high natural abundance, low toxicity, excellent photostability, suitable band edge potentials, and high absorption coefficient for ultraviolet (UV) radiation [4–6]. However, the light harvesting capability of TiO_2 is severely limited by its large bandgap [7]. Various approaches such as heteroatom doping [5], self-doping with Ti^{3+} [8], and the introduction of surface disorder [6] have been implemented to improve the visible-light activity of TiO_2. Among these strategies, heteroatom doping is currently the most commonly used method [5,9–11].

TiO_2 materials doped with non-metal elements such as nitrogen [5,10] and sulfur [11] have demonstrated visible-light responses. However, their visible-light photoactivities are still limited. In addition, the photocorrosion induced by the oxidation of the non-metal ion during water oxidation represents a major hurdle for their applications [10,11]. Recent theoretical calculations demonstrated that metal dopants (*e.g.*, Cr, Fe, and Co) can extend the range of absorption to the visible region and improve the photostability of TiO_2 [9,12]. Among these metal dopants, Cr was found to be effective in enhancing the visible-light absorption of TiO_2, due to its suitable ion radius and the position of its energy states within the forbidden band [13].

However, to date, the reported visible-light photoactivity of Cr doped TiO_2 is far lower than that of TiO_2 doped with non-metals [10,11]. This can be attributed to two main factors. First, it is difficult to incorporate metal ions in the TiO_2 lattice without aggregation using conventional chemical methods [14]. Second, metal doping may negatively affect the charge separation/transfer efficiency and, thus, the performance of the photoelectrode [2,15–17]. Therefore, an effective doping approach resulting in a metal-doped TiO_2 with favorable electronic properties and good visible-light photoactivities is highly desirable.

Ion implantation is a conventional material modification strategy that has been extensively used to modulate the electronic properties of semiconductors in the past decades. Compared with conventional chemical doping methods, ion implantation can incorporate virtually any metal-ion dopants of interest into the bulk lattice with controlled dose and depth. Additionally, the implanted metal ions are highly dispersed and isolated in the matrix material [18]. Herein, we employed an ion implantation method to dope Cr into TiO_2 nanowire arrays for PEC water oxidation. Although Cr doping effectively narrows the bandgap and significantly enhances the visible-light absorption of TiO_2, its visible-light photoactivity is still relatively low. Surprisingly, we found that post vacuum annealing played a decisive role in activating the visible-light photoactivity of Cr-doped TiO_2. A vacuum-treated Cr-doped TiO_2 (denoted as Cr-TiO_2-vac) with a Cr dose of 3×10^{16} cm^{-2} and subsequent vacuum annealing treatment at 550 °C for 3 h exhibited a visible-light (> 420 nm) current density of 0.53 mA/cm^2 at 1.8 V *vs.* reversible hydrogen electrode (RHE) without any other co-catalysts. A combination of experimental characterizations and theoretical calculations showed that the increased photoactivity can be attributable to the synergic effect of the Cr-dopant and oxygen vacancy that was created during vacuum

annealing, improving both the visible-light absorption and electrical conductivity of TiO_2. Furthermore, Cr-TiO_2-vac exhibited impressive photostability. There was almost no photocurrent decay after testing for 100 h.

2. Experimental

2.1. Sample preparation

Rutile TiO_2 NW arrays on FTO glass were synthesized using a well-developed hydrothermal method [19]. Briefly, 0.6 mL of titanium (IV) butoxide was added to 36 mL of an aqueous HCl solution (18 mL of deionized (DI) water + 18 mL of concentrated HCl (38%) with magnetic stirring). After stirring for 5 min, the solution was poured into a Teflon-lined stainless-steel autoclave (50 mL capacity). A piece of the FTO substrate (2.5×4 cm^2), which was cleaned for 60 min using an ultrasonicator in a mixed solution of DI water, acetone, and isopropanol (IPA), was immersed in the solution. The autoclave was sealed and heated to 150 °C for 8 h in an electric oven. The obtained samples were washed with DI water and finally annealed in air at 550 °C for 3 h. Chromium ions were implanted into the as-prepared TiO_2 NW arrays at 80 kV, with different ion dosages (1×10^{15}–5×10^{16} cm^{-2}), using a metal vapor vacuum arc (MEVVA) ion source implanter. The implanted samples were then annealed in vacuum or in air at 550 °C for 3 h.

2.2. Photoelectrochemical measurements

Photoelectrochemical (PEC) measurements were carried out in a conventional three-electrode system connected to a computer-controlled electrochemical workstation (CHI 650E) under a solar simulator (Abet technologies, SunLite^{TM} solar simulator, Model: 11002) at an irradiation intensity of 100 mW/cm^2 with and without a visible light cutoff filter ($\lambda > 420$ nm). The PEC reactor contained a photoanode, a Pt foil, and an Ag/AgCl/KCl (sat) electrode as the working, counter, and reference

electrodes, respectively. An aqueous solution of 1.0 M NaOH (pH = 13.6) was used as the electrolyte. IPCE spectra were obtained by using a xenon lamp (Newport model 66902) coupled with a grating monochromator (Newport Model 74125) and a power meter (Newport model 2936-R) with a photodiode (Newport model 71675_71580) in the wavelength range of 300–600 nm with an applied potential of 1.8 V (vs. RHE). The measured potentials *vs.* Ag/AgCl were converted to a reversible hydrogen electrode (RHE) scale according to the Nernst equation:

$$E_{RHE}\ (V) = E_{Ag/AgCl} + E^{o}_{Ag/AgCl} + 0.059 \times pH = E_{Ag/AgCl} + 1 \qquad (1)$$

where $E^{o}_{Ag/AgCl}$ = 0.1976 V at 25 °C, $E_{Ag/AgCl}$ is the experimentally measured potential against the Ag/AgCl reference electrode, and E_{RHE} is the converted potential vs. RHE.

2.3. Characterization

Field-emission scanning electron microscopy (FE-SEMs) was conducted using a JEOL S-4800 microscope. Transmission electron microscopy (TEM) and high-resolution transmission electron microscopy (HRTEM) were carried out on a Titan G2 60-300 Probe Cs Corrector high-resolution scanning transmission electron microscope (HRSTEM). X-ray diffraction patterns were collected on a Bruker AXS, D8 Advance X-ray powder diffractometer with Cu-K_α radiation (λ = 0.15418 nm). Raman measurement was performed on a laser confocal microRaman spectrometer (RenishawinVia, Renishaw) with laser excitation at 532 nm. UV–vis diffuse reflectance spectra (DRS) were recorded on a PerkinElmer Lambda 750 S spectrometer equipped with an integrating sphere. X-ray photoelectron spectroscopy (XPS) experiments were conducted on a Thermo Scientific ESCALAB 250Xi system with Al-K_α (1486.6 eV) as the radiation source. Peak positions were internally referenced to the C 1*s* peak at 284.8 eV. X-ray absorption near-edge structure (XANES) spectra were recorded at the BL10B beamline in the National Synchrotron

Radiation Laboratory (NSRL) in Hefei, China. Electron paramagnetic resonance (EPR) spectra were collected at room temperature using a JES-FA200 spectrometer. Samples of TiO_2, Cr-TiO_2-air, and Cr-TiO_2-vac nanowire powder were scraped from the growth substrates using a blade. We used the same amount of TiO_2, Cr-TiO_2-air, and Cr-TiO_2-vac samples for EPR and XANES characterizations.

2.4. Theoretical calculation

All calculations were performed with the CASTEP code as implemented in the Materials Studio package of Accelrys Inc. A high-level, reliable HSE06 (Heyd-Scuseria-Ernzerhof) hybrid functional was utilized, which improves the calculations for bandgaps, dielectric properties, and the equilibrium volume. The plane wave cutoff energy was 500 eV with a 3×3×5 Monkhorst-Pack special k-point grid for a 2×2×2 supercell for integration over the Brillouin zone. The norm-conserving pseudopotential was employed for the geometry optimizations and property calculations. The convergence tolerances were set to 5.0×10^{-6} eV per atom for energy, 5.0×10^{-4} Å for maximum displacement, and 0.01 eV $Å^{-1}$ for maximum force. The lattice parameters of rutile TiO_2 were a=4.61 Å and c=3.04 Å. The doping of Cr was based on a 2×2×2 supercell containing 8 primitive unit cells of rutile TiO_2 with a mole ratio of 1/15 for Cr/Ti, to obtain the structure $Ti_{33}Cr_2O_{40}$. Two types of oxygen vacancy defects were designed on the surface of Cr-doped TiO_2, including one connected with three Ti atoms and the other connected with one Cr atom and two Ti atoms.

3. Results and discussion

3.1. Structure characterization

TiO_2 nanowire (NW) arrays were grown on FTO glass using a well-developed hydrothermal approach [19]. Cr ions were implanted into TiO_2 by an ion implanter

and followed by a thermal treatment under vacuum, as shown in the material processing scheme in Fig. 1(a). SEM images (Fig. 1b) show that the FTO glass substrate was uniformly covered with vertically aligned Cr-TiO_2-vac NWs. Each NW has a rectangular cross section and a smooth surface facet. SEM images collected from freshly prepared TiO_2 NWs and Cr implanted TiO_2 NWs with air annealing treatment (Cr-TiO_2-air) further demonstrated that these modification methods do not change the morphology of the TiO_2 NW arrays (Fig. S1, Supporting Information). The crystallinity of the NWs was similar before and after Cr doping (Fig. S2, Supporting Information). Element mapping images show that Cr dopants are uniformly distributed over the TiO_2 NWs (Fig. 1c). The Cr/Ti mole ratio was estimated to be 2.29 at% *via* a quantitative analysis of the EDX spectrum (Fig. S3, Supporting Information).

X-ray diffraction (XRD) patterns indicate that all the samples exist in the rutile phase [19] (Fig. 1d). After Cr ion implantation, the intensity of the TiO_2 diffraction signals considerably decreased, suggesting that high-speed ion bombardment indeed creates defects in the TiO_2 host crystal structure. Significantly, the diffraction peak intensities of the rutile phase were recovered upon post-implantation annealing. The important role of heat treatment in repairing the lattice defects formed by ion bombardment was also confirmed by Raman spectroscopy. Four characteristic Raman-active modes of TiO_2 with frequencies at 142, 234, 446, and 609 cm^{-1} were observed (Fig. S4, Supporting Information), corresponding to the B_{1g}, multi-photon, E_g, and A_{1g} modes of the rutile space group ($P4_2/mnm$), respectively [20]. Similarly, the intensity of these vibrational peaks decreased after ion implantation, while the signals were recovered by the post-implantation annealing treatment. It is also noteworthy that a Raman-forbidden mode at approximately 690 cm^{-1} (forbidden A_{2g}

transition) [21] emerged for Cr-doped TiO_2, suggesting the occurrence of structural changes after Cr doping. High-resolution transmission electron microscopy (HRTEM) and fast Fourier transform (FFT) studies confirmed that the Cr-implanted TiO_2 NWs maintained good crystallinity (Fig. 1e).

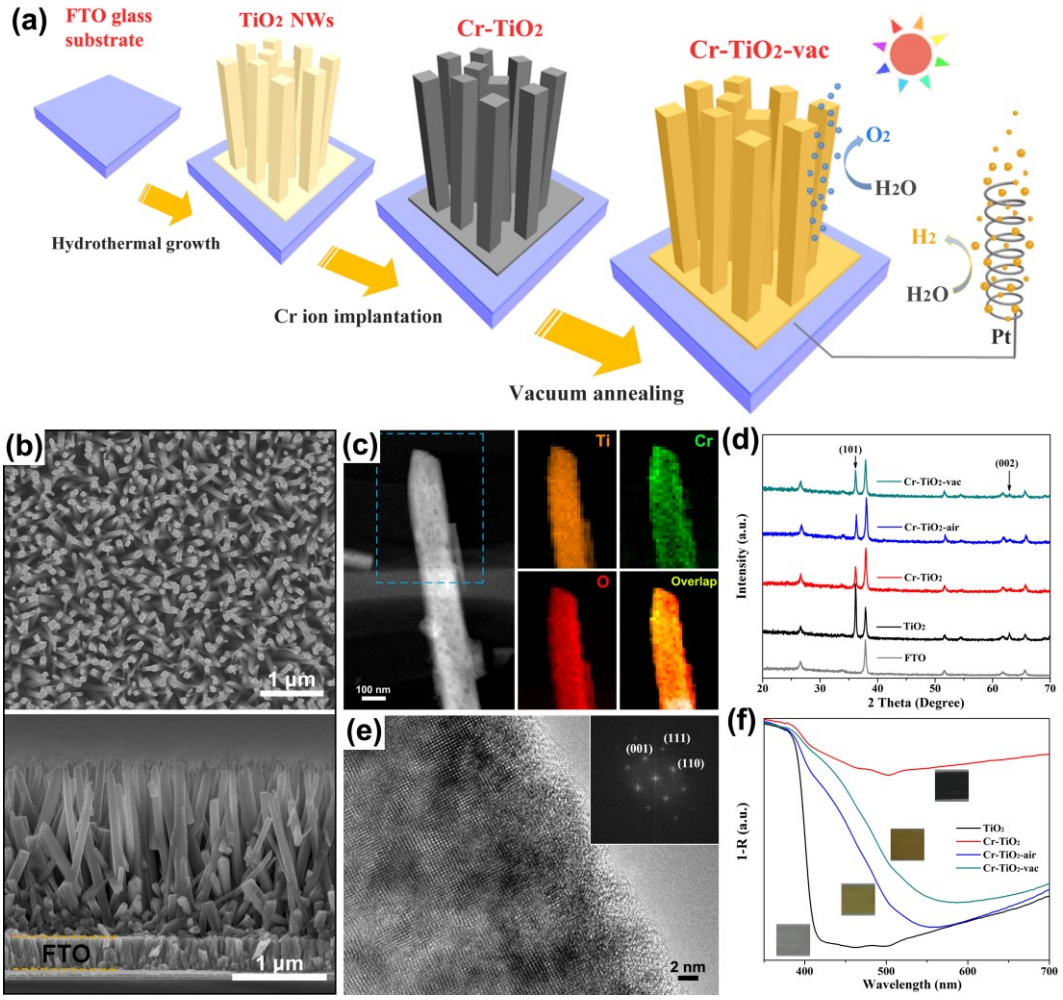

Fig. 1. (a) Schematic illustration of the fabrication process of Cr-TiO_2-vac NW photoanode. (b) SEM images of the top (upper panel) and the side (lower panel) of the Cr-TiO_2-vac NW arrays. (c) STEM images of a single Cr-TiO_2-vac NW and the corresponding energy-dispersive X-ray spectroscopy elemental mapping images of Cr, Ti, O and the overlapped mapping image. (d) XRD patterns of FTO, TiO_2, Cr-TiO_2, Cr-TiO_2-air, and Cr-TiO_2-vac. (e) HRTEM image of a Cr-TiO_2-vac NW. Inset: corresponding FFT pattern. (f) UV-vis absorption spectra of TiO_2, Cr-TiO_2,

Cr-TiO_2-air, and Cr-TiO_2-vac. Inset: photographs of these samples.

The photographs (Fig. 1f, inset) show that Cr ion implantation obviously changed the color of the TiO_2 films. The white pristine TiO_2 NWs was black after Cr implantation, which in turn became yellow and brownish yellow with a subsequent heat treatment under air and vacuum, respectively. Diffuse reflectance ultraviolet-visible spectra of these samples were acquired to analyze the light absorption properties. The unmodified TiO_2 only absorbs ultraviolet light below 410 nm, consistent with the observation for rutile TiO_2 [7]. However, the Cr-TiO_2, Cr-TiO_2-air, and Cr-TiO_2-vac samples exhibited a significant absorption from 400 to 600 nm, which could be ascribed to the localized Cr-dopant energy levels within the bandgap. Notably, the absorption edge of the Cr-TiO_2-vac sample showed a ~20 nm shift to the longer wavelength region as compared to the Cr-TiO_2-air sample. These results clearly indicate that both Cr ion implantation and subsequent annealing treatment can change the optical and electronic structure of TiO_2.

3.2. Chemical states analysis

X-ray photoemission spectroscopy (XPS) measurements were performed to probe the surface chemical states of Cr-implanted TiO_2. As shown in the XPS survey spectra (Fig. S5a, Supporting Information), all the samples exhibited Ti and O signals, as expected. Fairly weak Cr signals were observed in the Cr-implanted samples. C signals were believed to be included during the fabrication of the samples. No other elements were detected, demonstrating that ion implantation is a clean process that selectively doped TiO_2 only with the element of interest. Fig. 2(a) shows the XPS Cr 2*p* spectra of TiO_2, Cr-TiO_2-air, and Cr-TiO_2-vac. The signal centered at 580 eV corresponds to the Ti 2*s* plasmon loss satellite peak. Cr-TiO_2-air exhibited a peak at approximately 577.5 eV that can be assigned to Cr^{3+} [22]. Importantly, the peak

shifted to a lower binding energy in the Cr-TiO_2-vac sample, indicating the formation of some lower valent Cr species during vacuum annealing [22]. The Ti $2p_{3/2}$ signals were observed at 458.5, 458.2, and 458.1 eV for pristine TiO_2, Cr-TiO_2-air, and Cr-TiO_2-vac, respectively (Fig. 2b). The negative shift in binding energy also suggests that the Ti^{3+} species was possibly present on the surface of Cr-TiO_2-vac [10,15].

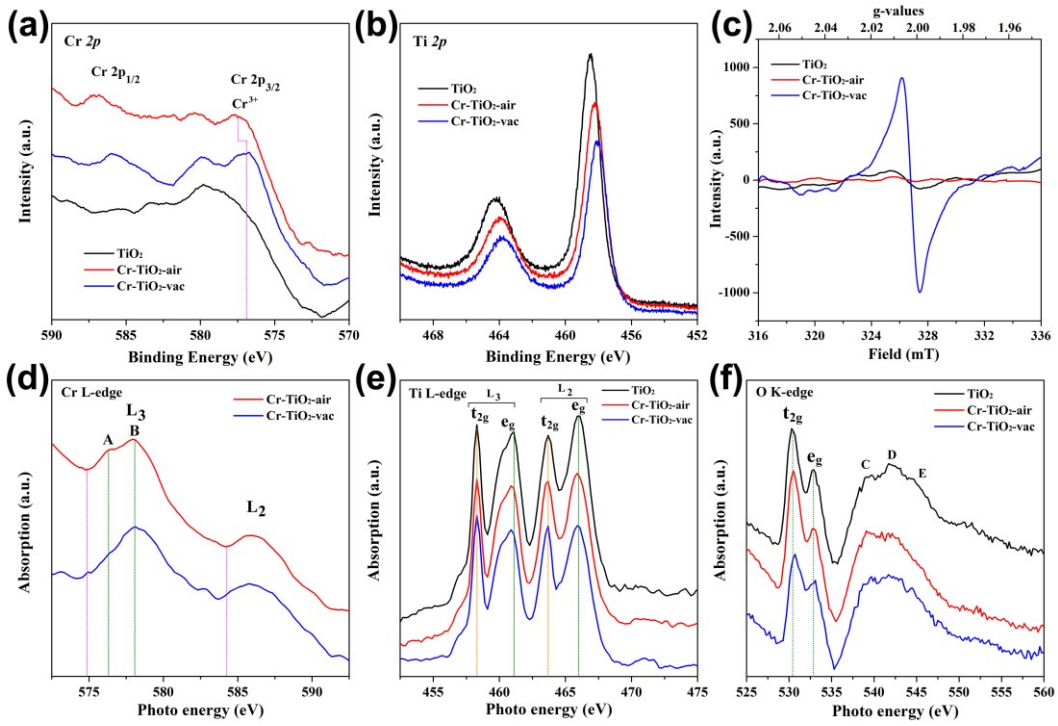

Fig. 2. (a) XPS Cr 2*p* spectra, (b) XPS Ti 2*p* spectra, and (c) EPR spectra of TiO_2, Cr-TiO_2-air, and Cr-TiO_2-vac NWs. (d) XANES spectra of Cr L-edge for Cr-TiO_2-air and Cr-TiO_2-vac NWs. (e) XANES spectra at the Ti L-edge and (f) O K-edge of TiO_2, Cr-TiO_2-air, and Cr-TiO_2-vac NWs.

In addition to the surface nature of the Cr-TiO_2-vac NWs, we also aimed to understand how the Cr ion implantation and post-implantation annealing affect the bulk structure of TiO_2. EPR was employed to characterize the chemical states in bulk TiO_2 [23]. The strong EPR signal obtained from Cr-TiO_2-vac with a g-value of 2.001 indicates the existence of oxygen vacancies [23], while only a trace amount of oxygen

vacancies was observed for pristine TiO_2 and Cr-TiO_2-air (Fig. 2c). We believe the abundant oxygen vacancies present in Cr-TiO_2-vac results in the increase in electron density around the metal atoms, causing the negative shift in binding energy observed for Ti and Cr in the XPS measurements.

X-ray absorption near-edge structure (XANES) spectra in the soft X-ray ranges were also collected to study the electronic structures of the Cr-doped TiO_2 samples (Fig. 2d-f). Fig. 2(d) shows the XANES Cr L-edge spectra of Cr-TiO_2-air and Cr-TiO_2-vac. Compared with the references of the Cr L-edge, peaks A and B can be ascribed to Cr^{3+} [24]. The Cr L-edge (L_3 and L_2) of Cr-TiO_2-vac has a lower absorption threshold than that of Cr-TiO_2-air (pink dotted line in Fig. 2d), indicating the presence of lower valent Cr species in the Cr-TiO_2-vac sample, in good agreement with the XPS Cr 2*p* results. The XANES Ti L-edge spectra of TiO_2, Cr-TiO_2-air, and Cr-TiO_2-vac are depicted in Fig. 2(e). Two doublet peaks (455–470 eV) for the Ti L-edge primarily originate from an electron transfer from the Ti $2p_{3/2}$ or $2p_{1/2}$ orbital to the Ti 3*d* orbital in TiO_2 (L_3 and L_2), which further splits into the t_{2g} and e_g orbitals in the octahedral symmetry arrangement. The first and second peaks of each doublet were assigned to the transfer to the t_{2g} and e_g orbitals, respectively [25,26]. Compared with pristine TiO_2, the L_3-edge e_g orbital of the Cr-implanted TiO_2 samples (Cr-TiO_2-air and Cr-TiO_2-vac) slightly shifted to a lower energy. The split energy between the t_{2g} and e_g orbitals reflects the symmetry in the first coordination shell of the Ti atoms, indicating that the implanted Cr ions caused a slight lattice distortion [26]. In the XANES O K-edge spectra (Fig. 2f), the two relatively sharp features (530–535 eV) corresponding to the electronic transitions from the O 1*s* orbital to the t_{2g} and e_g orbitals, were observed. The higher energy signal from 535 to 547 eV (peaks C, D and E) originates from the transitions from the O 1*s* orbital to the

hybridized orbitals induced by the antibonding Ti 4*sp* and O 2*p* orbitals [23]. We also found that the t_{2g} orbital of Cr-TiO_2-vac exhibited an obvious decrease in the absorption intensity and slightly shifted to a higher energy, as compared to pristine TiO_2 and Cr-TiO_2-air, indicating the existence of oxygen vacancies on its surface [23,25], again in good agreement with the XPS results.

3.3. DFT calculations

Density functional theory (DFT) calculations were performed to understand the separate effects of the Cr dopants and the oxygen vacancies (O_{vac}) as well as the possible interaction between the Cr dopant and O_{vac} on the electronic and optical properties of TiO_2. Fig. 3(a-d) respectively shows the structures of pristine TiO_2, Cr-doped TiO_2 (Cr-TiO_2), oxygen-deficient TiO_2 (O_{vac}-TiO_2), and Cr-doped and oxygen-deficient TiO_2 (Cr-O_{vac}-TiO_2) with the main charge values and the electron density difference. The charge distribution on Ti and O decreased after Cr doping (Cr-TiO_2) as the Cr-O interaction is weaker than the Ti-O interaction (Fig. 3a, b). Additionally, the state of oxygen vacancies in O_{vac}-TiO_2 (Fig. 3c) mainly spreads to the adjacent 5-coordinated Ti, which is attributed to the electron distribution on the e_g orbital of Ti pointing towards the oxygen vacancy site. It is noteworthy that the excess electrons generated by the oxygen vacancy only partially transfer to the adjacent atoms and still retain some charges at the oxygen vacancy sites (Fig. 3c). For Cr-O_{vac}-TiO_2, the charge distribution on Cr significantly decreased from 1.54 to 1.18, suggesting that the excess electrons on the oxygen vacancies changed the oxidation state of Cr (Fig. 3d). These results support the experimental observations of the negative shift in binding energy and lower absorption threshold in the XPS and XANES studies of the Cr-TiO_2-vac samples, respectively. The projected densities of the states of pristine TiO_2, Cr-TiO_2, O_{vac}-TiO_2, and Cr-O_{vac}-TiO_2 were also obtained

and displayed in Fig. 3(e). The bandgap of pristine TiO_2 was calculated to be 3.5 eV. By introducing Cr dopants into TiO_2, one impurity state below the conduction band minimum in the forbidden band was generated, which was mainly contributed by the Cr 3*d* orbital. This impurity state contributes to the observed visible-light absorption. However, the Fermi level of Cr-TiO_2 is still located at the valence band maximum (VBM), as compared to pristine TiO_2. This indicates that only the Cr 3*d* impurity state is localized in TiO_2, which does not act as an electron donor. For TiO_2 doped with oxygen vacancies, the Fermi level shifted up to the produced impurity state by the two excess electrons donated by the oxygen vacancy, which is consistent with the electron density difference results. The transfer of these two excess electrons from the oxygen vacancy to the Cr 3*d* state (Fig. 3d) resulted in a downward shift of the Cr 3*d* impurities states in TiO_2 and a further narrowing of the bandgap (Fig. 3e). The bandgap shift observed for Cr-doped TiO_2 and Cr-TiO_2-vac is consistent with the absorption properties shown in Fig. 1(f). Moreover, the excess electrons transferred from the vacancy resulted in an upward shift of the Fermi level to the Cr 3*d* state. As a result, the degree of band bending increased at the surface of TiO_2, thus facilitating charge separation [10,15]. These results revealed the synergistic effect between the oxygen vacancies and the Cr dopants on the modification of the electronic and optical properties of TiO_2.

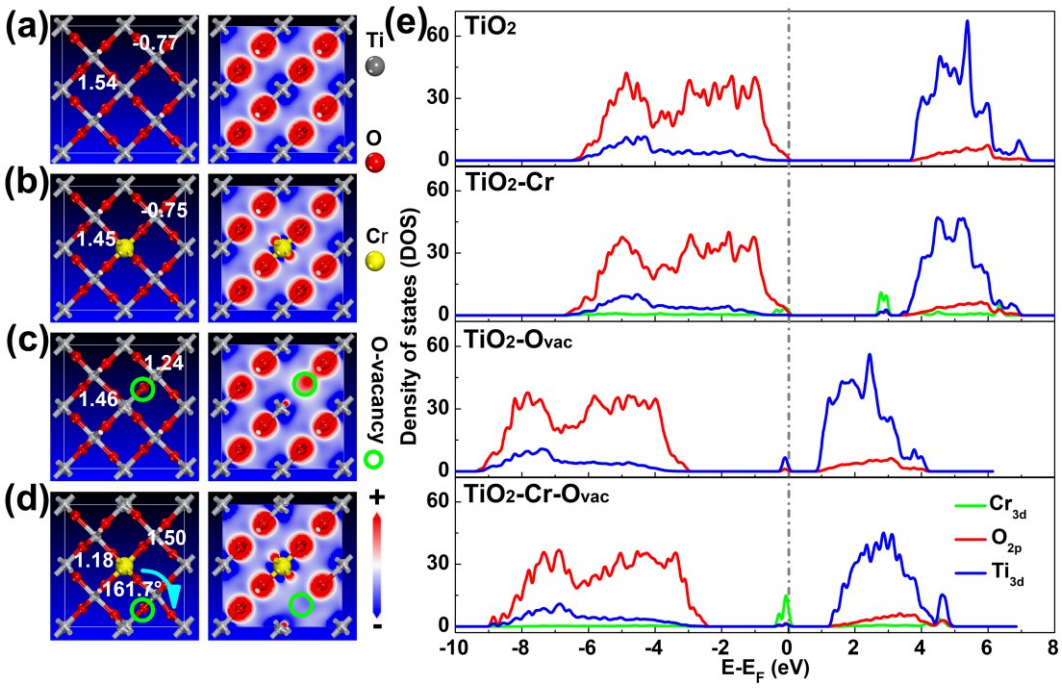

Fig. 3. (a-d) Structures and electron density differences of TiO_2, Cr-TiO_2, O_{vac}-TiO_2, and Cr-O_{vac}-TiO_2 with labeled charge distribution values and their (e) corresponding projected density of states (PDOS) plots. The dashed line is the Fermi level.

3.4. PEC performance characterization

PEC performances of the TiO_2 photoanodes were investigated under simulated solar illumination of 100 mW/cm^2, in a three-electrode configuration with the TiO_2 sample as the working electrode, Pt foil as the counter electrode and Ag/AgCl/KCl (sat) as the reference electrode, in a 1.0 M NaOH solution (pH = 13.6). Fig. 4(a) shows the results of chopped linear-sweep voltammetry (LSV) for the Cr-TiO_2-vac sample. Cr-TiO_2-vac achieved a photocurrent density of 1.29 mA/cm^2 at 1.8 V *vs.* RHE under simulated solar light illumination, which is three times higher than that of the pristine TiO_2 NWs (0.41 mA/cm^2) (Fig. 4a, inset) obtained at the same potential. Most importantly, the photocurrent density of Cr-TiO_2-vac reached 0.53 mA/cm^2

under visible-light (> 420 nm) illumination, which accounts for 41.1% of the total photocurrent density generated under simulated solar illumination. For pristine TiO_2, the photocurrent contributed from visible light is only about 0.5% at 1.8 V *vs.* RHE. Fig. 4(b) shows the *I-t* curves of TiO_2, Cr-TiO_2-air, and Cr-TiO_2-vac collected under chopped visible-light illumination at 1.8 V (*vs.* RHE). Among them, Cr-TiO_2-vac has the highest photocurrent density, which is 2 orders of magnitude higher than that of the pristine TiO_2 NWs. Cr-TiO_2-air surprisingly only showed a slightly higher visible-light photoactivity relative to pristine TiO_2, although it absorbs visible light, suggesting that the localized Cr 3*d* impurity states are inefficient in separating and transferring the visible-light induced carriers, in the absence of oxygen vacancies.

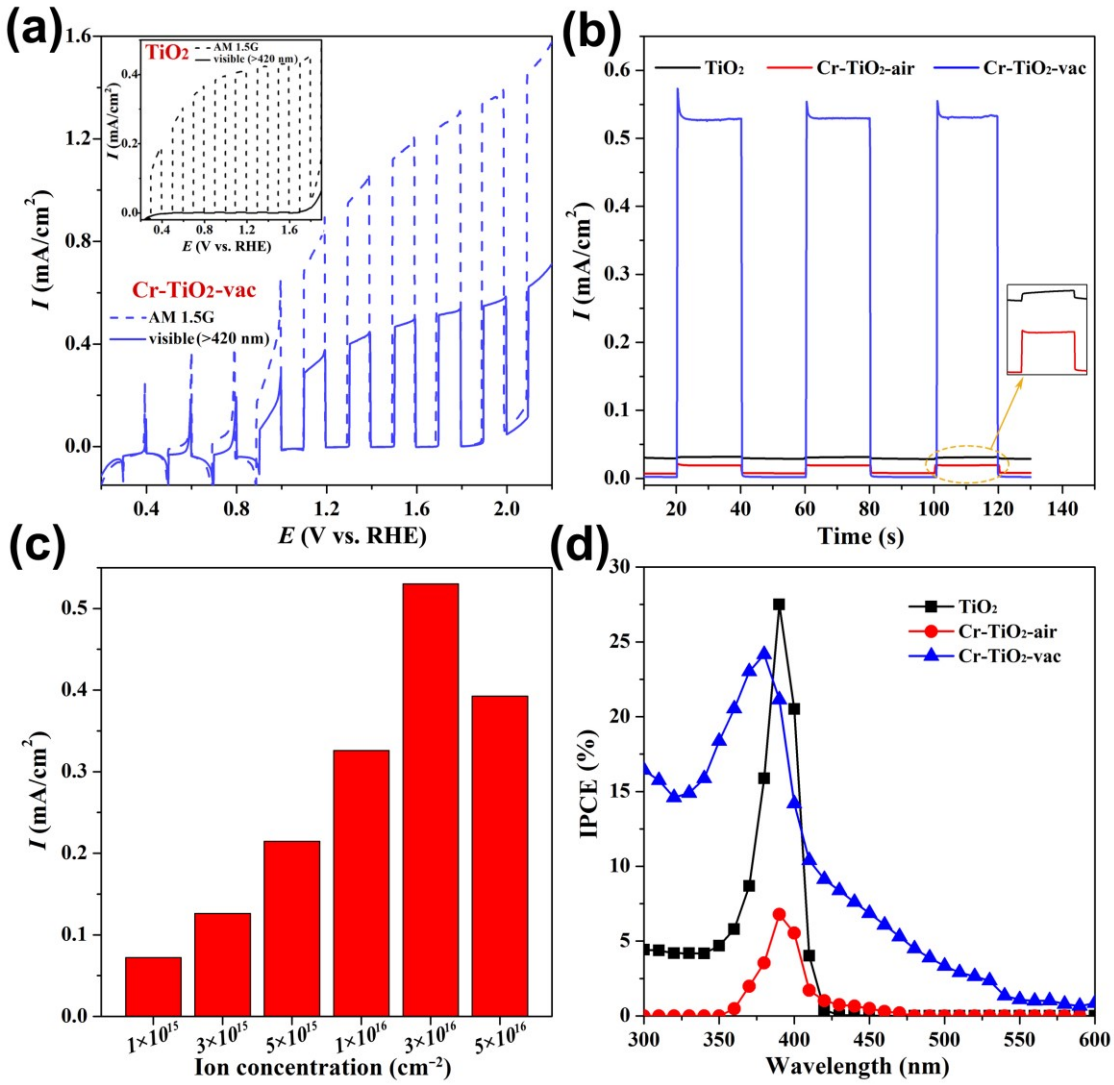

Fig. 4. (a) Chopped LSV of Cr-TiO_2-vac and pristine TiO_2 (inset). (b) Plot of photocurrent density of TiO_2, Cr-TiO_2-air, and Cr-TiO_2-vac under chopped visible-light (> 420 nm) illumination at 1.8 V *vs.* RHE as a function of time. (c) Histograms of the visible-light photocurrent density of Cr-doped TiO_2 NWs with different Cr doses collected at 1.8 V *vs.* RHE. (d) IPCE spectra obtained at 1.8 V *vs.* RHE.

Furthermore, we also evaluated the PEC performance of a series of TiO_2 samples at various Cr implantation dosages and vacuum annealing temperatures (Fig. 4c and Fig. S6, Supporting Information). The Cr-TiO_2-vac photoanodes with an implantation

ion fluence of 3×10^{16} cm^{-2} and followed by a vacuum annealing temperature of 550 °C showed the maximum photocurrent density. Further increases in the Cr ion dose or vacuum annealing temperature caused a reduction in photoactivity. Numerous recombination centers created by excessive Cr doping can be introduced into TiO_2. Additionally, annealing temperatures beyond 550 °C can severely damage the electrical conductivity and morphology of the FTO substrate. Moreover, a pristine TiO_2 NW sample annealed in vacuum under the same conditions (TiO_2-vac) was prepared and tested as a control sample. The *I-t* curves of TiO_2-vac are given in Fig. S7, Supporting Information. The sample exhibited a comparable photocurrent density as that of the pristine TiO_2 sample. These results further demonstrated that the increased visible-light photoactivity of Cr-TiO_2-vac is associated with the synergic effect of oxygen vacancies and Cr doping.

To understand the wavelength dependent photoactivity, we performed IPCE measurements (Fig. 4d). The IPCE values were calculated according to the equation IPCE = $(1240 \times I)/(\lambda \times J_{light})$, in which I is the measured photocurrent density, λ represents the wavelength of the incident light, and J_{light} is the measured irradiance density. The maximum IPCE of pristine TiO_2 was 27.5% at 390 nm with the response wavelength at approximately 420 nm, corresponding with the reported results for rutile TiO_2 [7]. Significantly, Cr-TiO_2-vac exhibited a substantially enhanced UV-light IPCE and remarkable visible-light photoactivity, as compared to pristine TiO_2. Cr-TiO_2-vac achieved an IPCE of ~6.8% at 450 nm, representing one of the highest values among all reported metal-ion doped TiO_2 based photoanodes without co-catalysts. The IPCE profile of the Cr-TiO_2-vac sample also fits well with its diffuse reflectance spectrum, confirming that the active photoactivity is indeed extended to ~540 nm. On the other hand, we observed a steep decrease in photoactivity in the

entire UV-light region for the Cr-TiO_2-air sample, suggesting that Cr doping alone can negatively affect the PEC performance of TiO_2. The Cr-TiO_2-air sample displayed negligible IPCE values in the visible-light region, again suggesting that oxygen vacancies are essential for the increased visible-light photoactivity of Cr-TiO_2-vac.

3.5. Electrochemical and photostability characterization

While the PEC performance depends on light absorption, charge separation and transport play decisive roles in the photoelectrochemical process [10,27]. To understand how the oxygen vacancies and Cr doping affect the charge separation and transport efficiency, electrochemical impedance studies were performed. Positive slopes of the Mott-Schottky curves from TiO_2, Cr-TiO_2, and Cr-TiO_2-vac indicate all these samples are *n*-type semiconductors, as expected (Fig. 5a). Importantly, a smaller slope observed for Cr-TiO_2-vac, as compared to pristine TiO_2 and Cr-TiO_2-air, suggests a higher donor density in the Cr-TiO_2-vac samples. The donor density can be obtained from the Mott-Schottky plots according to the equation $N_d = (2/e_0\varepsilon\varepsilon_0)[d(1/C^2)/dV]^{-1}$, in which e_0, ε, ε_0, N_d, C, and V respectively represent the electron charge, dielectric constant (ε=170) [15], permittivity of vacuum, donor density, space charge capacitance, and electrode potential. A carrier density of 1.95×10^{19} cm^{-3}, more than 2 orders of magnitudes higher than pristine TiO_2 (1.53×10^{17} cm^{-3}), was achieved in the Cr-TiO_2-vac samples. Since the Mott-Schottky equation was derived from the flat electrode model, it is expected to produce errors in determining the absolute value of the carrier density for nanostructured electrodes. Nevertheless, a qualitative comparison of the Mott-Schottky slopes (donor densities) of the different samples is reasonable because there was no obvious change in the NW morphology after both Cr ion implantation and the annealing treatment. The increased donor density is mainly attributed to the formation of oxygen vacancies, which serves

as a shallow donor in TiO_2, consistent with DFT calculations, as shown in Fig. 3(e) and previous reports [28]. Charge transfer properties of these samples were further tested by electrochemical impedance spectroscopy (EIS) measurements. Fig. 5(b) shows that the Nyquist curves of all the samples exhibited single capacitive arcs. By fitting the data to a typical Randles circuit (upper inset, Fig. 5b), Cr-TiO_2-vac was found to exhibit the smallest value of charge transfer resistance (R_{CT}) (Table 1). These results indicate that vacuum treatment significantly decreased the charge transfer resistance at the interface between the photoelectrode and electrolyte. By contrast, the Cr-TiO_2-air samples exhibited strong visible-light absorption and a higher carrier density than that of pristine TiO_2, although they have almost equal charge transfer resistances (Fig. 5b). The results showed that the effect of Cr dopants alone on charge transfer is minimal, while the presence of oxygen vacancies on the TiO_2 surface is critical. A recent study reported that surface defects such as oxygen vacancies can lead to the formation of surface hydroxyl species, which can further mediate the transfer of photoinduced holes from the metal oxide to water [29].

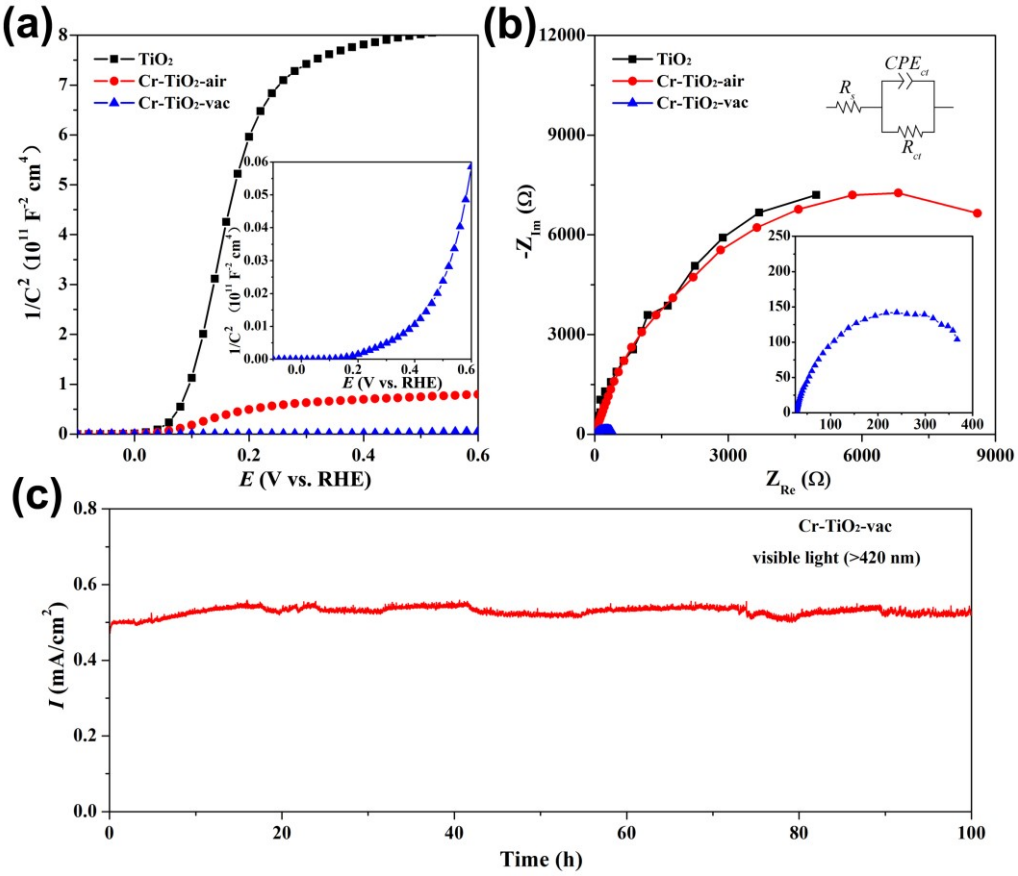

Fig. 5. (a) Mott–Schottky curves collected at a frequency of 1 kHz in the dark. Inset: magnified Mott–Schottky curve of Cr-TiO_2-vac. (b) Nyquist plots obtained at a potential of 1 V (*vs.* RHE) under simulated solar illumination. Inset: magnified Nyquist plot of the Cr-TiO_2-vac NWs. (c) Plot of the photocurrent density of Cr-TiO_2-vac obtained at 1.8 V (*vs.* RHE) for 100 h under visible-light illumination.

Photostability has been a major concern for element-doped TiO_2 materials. Therefore, we performed a long-term stability test for Cr-TiO_2-vac under visible-light illumination with a fixed potential of 1.8 V *vs.* RHE (Fig. 5c). Fig. S8 (Supporting Information) shows a digital picture of the PEC cell for the test. Gas evolution was observed at both the photoanode and Pt cathode. Significantly, Cr-TiO_2-vac did not show obvious photocurrent decays and morphology changes (Fig. S9, Supporting Information) under continuous light illumination for 100 h, performing much better

than N-implanted TiO_2 which was reported to lose 60% of its initial photocurrent after 1 week [10].

Table 1. Relative parameters obtained from Mott–Schottky, EIS, voltammetry, and IPCE measurements.

Sample	N_d[a] (cm^{-3})	R_{CT}[b] (Ω)	$j_{ph,\ visible}$[c] (mA cm^{-2})	IPCE[d] at 450 nm (%)
TiO_2	1.53×10^{17}	11340	0.002	0.01
Cr-TiO_2-air	2.29×10^{18}	10570	0.012	0.50
Cr-TiO_2-vac	1.95×10^{19}	238	0.53	6.86

[a]N_d was calculated from Fig. 5(a). [b]R_{CT} was estimated from Fig. 5(b). [c]$j_{ph,\ visible}$ was obtained at 1.8 V (*vs.* RHE) from Fig. 4(b). [d]IPCE at 450 nm was obtained from Fig. 4(d).

4. Conclusions

In summary, we demonstrated that Cr-ion implantation followed by a vacuum annealing process can significantly improve the visible-light photoactivity of TiO_2 photoanodes. The Cr-TiO_2-vac sample without the addition of any co-catalysts yielded a 0.53 mA/cm^2 visible-light photocurrent density and an IPCE of 6.8% at 450 nm at 1.8 V *vs.* RHE, which is one of the best values reported for metal ion-doped TiO_2 photoanodes. Notably, Cr-TiO_2-vac showed almost no photocurrent decay after 100 h under visible-light illumination. The combination of electrochemical studies and DFT calculations revealed that the remarkable visible-light photoactivity of Cr-TiO_2-vac is due to the synergistic interaction between the Cr dopants and oxygen vacancies. Specifically, the Cr dopants enhance visible-light absorption by introducing impurity levels within the bandgap of TiO_2, while the oxygen vacancies function as shallow donors that increase the carrier density and facilitate the

separation and transport of photoinduced carriers. In addition, this work demonstrated that ion implantation is a powerful method for the introduction of controlled numbers of dopants into the TiO_2 host crystal structure. The capability to control the dopant concentration enables the quantitative investigations of the doping effect, and the interaction between dopants and defects, such as oxygen vacancies. Nevertheless, this work also has room for improvement from a practical perspective. The high concentration of Cr doping results in a smaller photovoltage, which negatively affects the performance of the Cr-TiO_2 photoanode at low bias. While the introduction of oxygen vacancies improves the visible-light activity and charge transfer of the Cr-TiO_2 samples, it has little effect on their turn on potentials. To improve the low bias performance, Cr-TiO_2-vac could couple with suitable oxygen evolution catalysts.

Declaration of Competing Interest

The authors declare that they have no known competing financial interests or personal relationships that could have appeared to influence the work reported in this paper.

Acknowledgments

This work was financially supported by the National Natural Science Foundation of China (U1867215, 11722543, 11875211, U1932134), the Suzhou Key Industrial Technology Innovation Project (SYG201828), the Hubei Provincial Natural Science Foundation (2019CFA036), the Fundamental Research Funds for the Central Universities (2042020kf0211). Y.L. thanks the financial support from the National Science Foundation (U.S.) under grant no. DMR-2003563.

Supplementary material

Supplementary material associated with this article can be found in the online version.

References

[1] J. Montoya, L. Seitz, P. Chakthranont, A. Vojvodic, T. Jaramillo, J. Norskov, *Nat. Mater.*, 16 (2017) 70-81.

[2] S. Warren, K. Voitchovsky, H. Dotan, C. Leroy, M. Cornuz, F. Stellacci, C. Hebert, A. Rothschild, *Nat. Mater.*, 12 (2013) 842-849.

[3] T. Kim, K. Choi, *Science*, 343 (2014) 990-994.

[4] J. Gu, Y. Yan, J. Young, K. Steirer, N. Neale, J. Turner, *Nat. Mater.*, 15 (2016) 456-460.

[5] R. Asahi, T. Morikawa, T. Ohwaki, K. Aoki, Y. Taga, *Science*, 293 (2001) 269-271.

[6] X. Chen, L. Liu, P. Yu, S. Mao, *Science*, 331 (2011) 746-750.

[7] D. Scanlon, C. Dunnill, J. Buckeridge, S. Shevlin, A. Logsdail, S. Woodley, C. Catlow, M. Powell, R. Palgrave, I. Parkin, G. Watson, T. Keal, P. Sherwood, A. Walsh, A. Sokol, *Nat. Mater.*, 12 (2013) 798-801.

[8] L. Li, J. Yan, T. Wang, Z. Zhao, J. Zhang, J. Gong, N. Guan, *Nat. Commun.*, 6 (2015) 5881.

[9] Y. Zhao, C. Li, S. Lu, L. Yan, Y. Gong, L. Niu, X. Liu, *Chem. Phys. Lett.*, 647 (2016) 36-41.

[10] G. Wang, X. Xiao, W. Li, Z. Lin, Z. Zhao, C. Chen, C. Wang, Y. Li, X. Huang, L. Miao, C. Jiang, Y. Huang, X. Duan, *Nano Lett.*, 15 (2015) 4692-4698.

[11] C. Yang, Z. Wang, T. Lin, H. Yin, X. Lü, D. Wan, T. Xu, C. Zheng, J. Lin, F. Huang, X. Xie, M. Jiangl, *J. Am. Chem. Soc.*, 135 (2013) 17831-17838.

[12] Y. Gai, J. Li, S. Li, J. Xia, S. Wei, *Phys. Rev. Lett.*, 102 (2009) 036402.

[13] C. Cheney, P. Vilmercati, E. Martin, M. Chiodi, L. Gavioli, M. Regmi, G. Eres, T. Callcott, H. Weitering, N. Mannella, *Phys. Rev. Lett.*, 112 (2014) 036404.

[14] I. Cho, C. Lee, Y. Feng, M. Logar, P. Rao, L. Cai, D. Kim, R. Sinclair, X. Zheng, *Nat. Commun.*, 4 (2013) 1723.

[15] G. Wang, H. Wang, Y. Ling, Y. Tang, X. Yang, R. Fitzmorris, C. Wang, J. Zhang, Y. Li, *Nano Lett.*, 11 (2011) 3026-3033.

[16]H. Li, Y. Wu, C. Li, Y. Gong, L. Niu, X. Liu, Jiang, C. Sun, S. Xu, *Appl. Catal. B-Environ.*, 251 (2019) 305-312.

[17]X. Song, W. Li, D. He, H. Wu, Z. Ke, C. Jiang, G. Wang, X. Xiao, *Adv. Energy Mater.*, 8 (2018) 1800165.

[18] M. Anpo, M. Takeuchi, *J. Catal.*, 216 (2003) 505-516.

[19] B. Liu, E. Aydil, *J. Am. Chem. Soc.*, 131 (2009) 3985-3990.

[20] P. Narayanan, *Proceedings-Mathematical Sciences*, 32 (1950) 279-283.

[21] M. Ocaña, V. Fornés, J. Ramos, C. Serna, *J. Solid State Chem.*, 75 (1988) 364-372.

[22] M. Biesinger, B. Payne, A. Grosvenor, L. Lau, A. Gerson, R. Smart, *Appl. Surf. Sci.*, 257 (2011) 2717-2730.

[23]J. Xue, X. Zhu, Y. Zhang, W. Wang, W. Xie, J. Zhou, J. Bao, Y. Luo, X. Gao, Y. Wang, L. Jiang, S. Sun, C. Gao, *ChemCatChem*, 8 (2016) 2010-2014.

[24] D. Grolimund, T. Trainor, J. Fitts, T. Kendelewicz, P. Liu, S. Chambers, B. Jr, *J. Synchrotron Radiat.*, 6 (1999) 612-614.

[25] V. Lusvardi, M. Barteau, J. Chen, J. Jr, B. Frühberger, A. Teplyakov, *Surf. Sci.*, 397 (1998) 237-250.

[26] R. Brydson, H. Sauer, W. Engel, J. Thomas, E. Zeitler, N. Kosugi, H. Kuroda, *J. Phys.-Condens. Mater.*, 1 (1989) 797-812.

[27] Y. Yang, J. Gu, J. Young, E. Miller, J. Turner, N. Neale, M. Beard, *Science*, 350 (2015) 1061-1065.

[28] A. Janotti, J. Varley, P. Rinke, N. Umezawa, G. Kresse, C. Van de Walle, *Phys. Rev. B*, 81 (2010) 085212.

[29] C. Tang, B. Sun, M. Li, J. Zhang, X. Fan, F. Gao, Y. Tong, L. Dong, Y. Li, *J. Mater. Chem. A*, 7 (2019), 8050-8054.

Graphical Abstract

The introduction of oxygen vacancies activates the visible-light photoactivity of chromium-doped TiO_2 by enhancing the efficiency of charge separation and transfer.